Mineralogical Magazine, August 2018, Vol. 82(4), pp. 943–960

The fingerprint of imperial topaz from Ouro Preto region (Minas Gerais state, Brazil) based on cathodoluminescence properties and composition

Teodoro Gauzzi[1,*], Leonardo Martins Graça[1], Leonardo Lagoeiro[3], Isolda de Castro Mendes[2] and Gláucia Nascimento Queiroga[1]

[1] Department of Geology, Federal University of Ouro Preto, Ouro Preto, MG 35400-000, Brazil
[2] Department of Chemistry, Federal University of Minas Gerais, Belo Horizonte, MG 31270-901, Brazil
[3] Department of Geology, Federal University of Paraná, Curitiba, PR 81531-980, Brazil

[*Received 11 January 2017; Accepted 3 October 2017; Associate Editor: Martin Lee*]

ABSTRACT

A study of the cathodoluminescence (CL) properties of imperial topaz from Ouro Preto region (Minas Gerais state, Brazil) and its relation with trace-element composition was conducted, using scanning electron microscope cathodoluminescence (SEM-CL), optical microscope cathodoluminescence (OM-CL), cathodoluminescence-spectrometry (CL-spectrometry), electron microprobe analysis (EMPA), laser ablation inductively-coupled plasma mass spectrometry (LA-ICP-MS) and Raman spectrometry. Each analytical technique allowed characterization of the imperial topaz fingerprint. SEM-CL panchromatic images show different crystal growth and resorption events in imperial topaz crystals. Colour CL images indicate only blue to violet emissions. The CL-spectra indicate a broad emission band with low intensity peak at ~417 nm and a broad emission band with high intensity and major peaks at 685, 698, 711 and 733 nm. The EMPA indicates high OH content, in which the OH/(OH + F) ratio ranges between 0.35–0.43 ($0.72 \leq OH \leq 0.86$ apfu). High Cu and Zn concentrations (LA-ICP-MS) were measured in the high luminescence areas of SEM-CL images, suggesting both elements as CL-activators in imperial topaz. Raman and CL-spectra indicate high Cr concentrations, corroborated by EMPA and LA-ICP-MS results. The high Cr caused strong luminescence intensities that enabled their superimposition over the OH stretching mode (~3650 cm^{-1}) of topaz in all Raman spectra. Among trace elements, the concentrations of Ti, V, Cr, Mn, Fe, Cu, Zn, Ga and Ge provide the fingerprint of imperial topaz.

Keywords: imperial topaz, Ouro Preto, trace elements, cathodoluminescence.

Introduction

Topaz is a F/OH-bearing nesosilicate, $Al_2SiO_4(F,OH)_2$, that is usually found as an accessory and late-stage crystallization mineral in a wide variety of geological settings, such as F-rich felsic magmatic (rhyolites and granites) rocks, late-magmatic rocks (pegmatites) and post-magmatic rocks (greisens), hydrothermal veins and also in high-temperature and high- to ultrahigh-pressure metamorphic rocks, especially kyanite topaz-bearing quartzites (Zhang *et al.*, 2002; Marshall and Walton, 2007; Agangi *et al.*, 2014, 2016).

Topaz crystallizes in the orthorhombic system within the *Pbnm* space group. Its crystal structure consists of crankshaft chains of edge-sharing $[AlO_4(F,OH)_2]$-octahedra connected by isolated $[SiO_4]$-tetrahedra, which run parallel to [001]. It is also characterized by a combination of cubic and hexagonal close packing, perpendicular to [010], in which OH-anion layers alternate with and F-anion layers (Gaines *et al.*, 1997; Alberico *et al.*, 2003; Schott *et al.*, 2003; Gatta *et al.*, 2006).

*E-mail: teodoro.gauzzi@hotmail.com
https://doi.org/10.1180/minmag.2017.081.078

The major-element composition of topaz is fairly constant and its variation is only related to the OH/F concentration ratio (Skvortsova *et al.*, 2013). The OH content in topaz does not usually exceed $X_{OH} < 0.50$ [$X_{OH} = OH/(F + OH)$], due to the 'proton-proton avoidance', observed by Barton (1982). However, the studies carried out by Zhang *et al.* (2002) with topaz crystals of high- to ultrahigh-pressure metamorphic rocks (kyanite topaz-bearing quartzites) from Sulu terrane (Eastern China), have showed $0.35 \leq X_{OH} \leq 0.55$. With respect to the trace-element composition of topaz, other studies show significant variations in Ti, V, Cr, Mn, Fe, Cu, Zn, Ga and Ge (Leroy *et al.*, 2002; Wasim *et al.*, 2011; Wu *et al.*, 2011; Breiter *et al.*, 2013; Agangi *et al.*, 2014, 2016).

Imperial topaz is an orange-yellow to cherry-red variety of topaz that was reported in the Ouro Preto region, Minas Gerais state, Brazil, in the 18th century (Silva and Ferreira, 1987). A study on topaz from Ouro Preto, applying EMPA (electron microprobe analyses) and EPR (electron paramagnetic resonance), detected elements such as Ti^{3+}, Ti^{4+}, V^{4+}, Cr^{3+}, Mn^{3+} and Fe^{3+} (Schott *et al.*, 2003). However, the imperial topaz fingerprint has not been determined definitively. In order to characterize it, four samples from Dom Bosco mine (Ouro Preto, Brazil) were analysed with the following techniques: cathodoluminescence (CL), including scanning electron microscope cathodoluminescence (SEM-CL), coloured optical microscope cathodoluminescence (OM-CL), cathodoluminescence spectrometry (CL-spectrometry); EMPA; laser ablation inductively-coupled plasma mass spectrometry (LA-ICP-MS); and Raman spectroscopy. Cathodoluminescence will permit the identification of defects in the structure of topaz. These defects can be related to lattice defects (vacancies, broken bonds, etc.) or to the incorporation of some trace elements in the crystal structure of topaz. Also, CL enables the visualization of textures which are not observed by other methods, such as transmitted light microscopy, and backscattered electron (BSE), secondary electron (SE) and SEM imaging. EMPA and LA-ICP-MS will enable the quantitative elemental analysis of topaz. These techniques will provide the major- and trace-element compositions, respectively. In our study, EMPA will be important to understand the OH/F ratio in imperial topaz and if there is any relation of these elements with the CL-intensity in imperial topaz. LA-ICP-MS will be important to understand whether some trace elements activate CL in topaz, and how the concentrations of these trace elements may relate to high CL-intensity. Raman will enable observation of the molecular structure of topaz, especially the vibrational and stretching modes of $[SiO]_4$-tetrahedra and $[AlO_6]$-octahedra, and the behaviour of the OH stretching mode in imperial topaz.

Geological setting

The Ouro Preto region is located in the Southeast of Minas Gerais state, Brazil, and is geologically related to the Quadrilátero Ferrífero District. The Quadrilátero Ferrífero (Iron Quadrangle) is a greenstone terrain, where rocks of predominantly Archaean and Proterozoic age outcrop in a dome-and-keel style (Alkmim and Marshak, 1998). The basement of the supracrustal unit consists of domes of gneissic-granitic-migmatite rocks that formed over a time-span ranging from 3200 to 2900 Ma (Machado and Carneiro, 1992; Lana *et al.*, 2013). The supracrustal rocks are metavolcanic and metasedimentary units of the Supergroup Rio das Velhas and the Minas Supergroup (Machado *et al.*, 1992; Renger *et al.*, 1995; Noce *et al.*, 1998). The former is composed mainly of ultramafic-mafic metamorphosed rocks and by metasedimentary units including the Algoma-type Iron Formation and volcanic-clastic rocks. Overlying these Archaean rocks is the Minas Supergroup. The Minas Supergroup is composed of the Caraça, Itabira, Piracicaba and Sabará groups (Dorr II, 1969; Alkmim and Marshak, 1998; Lana *et al.*, 2013). The base of this supergroup consists of metasedimentary rocks of clastic and chemical origin. Among them are thick layers of iron formation rocks as well as carbonate units (Renger *et al.*, 1995). On the top of this sequence is the Piracicaba Group, which consists typically of 2420 Ma metaquartzites, phyllites, metagraywackes, carbonate-bearing phyllites and dolomitic marbles (Dorr II, 1969; Gandini, 1994; Babinski *et al.*, 1995). These Piracicaba Group rocks hosted the mineralization of imperial topaz which occurs mainly in the Ouro Preto region. The imperial topaz mineralization occurs as topaz-bearing veins which essentially crosscut the altered phyllites of the Piracicaba Group rocks and along the Northeastern area of the Dom Bosco Syncline hinge zone and is associated with the Brasiliano tectonothermal event at ~600 Ma (Dorr II, 1969; Morteani *et al.* 2002). Due to the tropical weathering, the imperial topaz-bearing veins occur within a halo of strongly altered rock (Fig. 1) in the crosscut phyllites, which are intensively altered. This alteration produces a brownish clay-like material, locally designated by

https://doi.org/10.1180/minmag.2017.081.078 Published online by Cambridge University Press

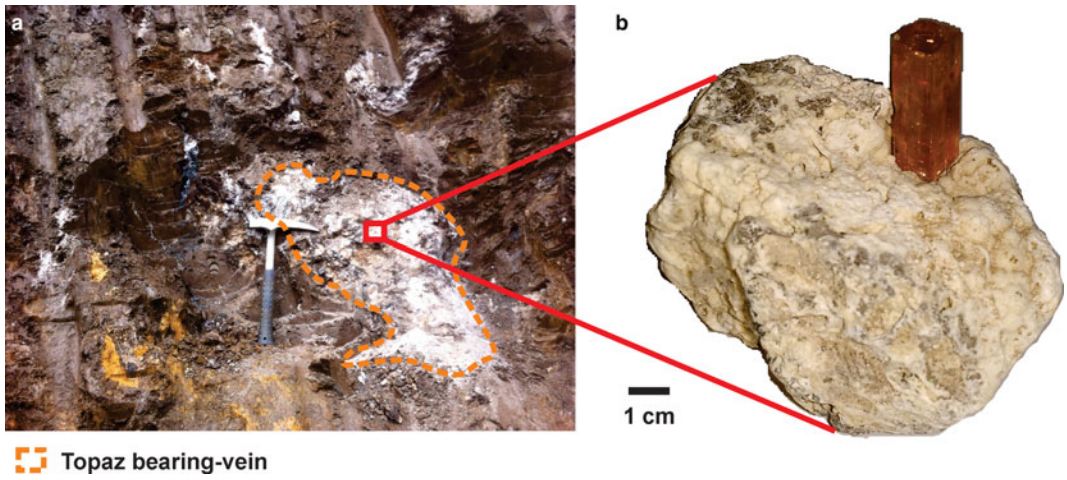

FIG. 1. Intensively altered phyllites from the Piracicaba Group rocks, at Dom Bosco mine: (*a*) an imperial topaz-bearing vein crosscutting the brown terrena; (*b*) a vein containing a crystal of imperial topaz.

the miners as 'borra de café' or brown terrena (Olsen, 1971). Due to this very intense alteration, there is no reliable information about the primary country rock related to the imperial topaz mineralization. In addition, topaz-bearing veins are mineralogically composed of kaolinite, quartz, mica, rutile and, rarely, euclase (Gandini, 1994; Morteani *et al.*, 2002).

The imperial topaz occurs in hydrothermal veins, whose genesis is assigned to a mineralizing fluid that resulted from a metamorphic tectonothermal event, during the Brasiliano orogeny, at ~600 Ma (Morteani *et al.*, 2002). In agreement with this study, the imperial topaz would have crystallized from *P-T* conditions of 3.50–5.00 kbar and 360 ± 7.00°C. The minimum value for pressure was obtained from the temperature of homogenization of CO_2–H_2O fluid inclusions (Gandini, 1994). The maximum value for pressure was estimated by Wunder *et al.* (1993, 1999), for high-pressure crystallization of OH-topaz. In the study carried out by Morteani *et al.* (2002), the temperature was obtained by oxygen isotope thermometry for the quartz and hematite intergrowth with imperial topaz; the mentioned intergrowth is assumed to be related to equilibrium among the three mineral phases. Also in agreement with the aforementioned authors, the *P-T* conditions are within the stability field of pyrophyllite and kaolinite, which are both present as inclusions in imperial topaz.

Sample description and preparation

The samples are from the Dom Bosco mine, specifically from the Dom Bosco Syncline area, Ouro Preto region, and were named DB-1, DB-2, DB-3 and DB-4 (Fig. 2). The selected samples showed a prismatic habit, essentially euhedral, and with 'striae' along the well preserved lateral faces, parallel to the *c* axis, and were mainly free of inclusions. The colours and dimensions (width × height in mm) of the samples are: DB-1, orange-pinkish, 6.00 x 10.00; DB-2, yellowish, 2.50 x 4.00; DB-3, orange-pinkish, 11.50 x 15.00; DB-4, orangish, 6.00 x 12.00. All these samples were cut parallel to (001) and perpendicular to the *c* axis. After this procedure, the samples were mounted in an epoxy resin, then polished using a 0.25 μm diamond powder until the imperial topaz crystals had been exposed. The samples were cleaned with HNO_3 before analysis in order to avoid contamination.

Methods

Cathodoluminescence (CL)

Panchromatic SEM-CL images were obtained using a JEOL JSM-6510 equipped with a CL detector, with a wavelength range of 200–800 nm, in the Microanalysis Laboratory of the Department of Geology at the Federal University of Ouro Preto (Brazil). The accelerating voltage was 20 kV.

Colour optical microscope-cathodoluminescence (OM-CL) images were obtained using a CITL Mk2 consisting of a cooled charge-coupled device (CCD) camera, a cold cathode discharge tube and a vacuum chamber at the Technological Characterization Laboratory (SCT) of the Centre of Mineral

https://doi.org/10.1180/minmag.2017.081.078 Published online by Cambridge University Press

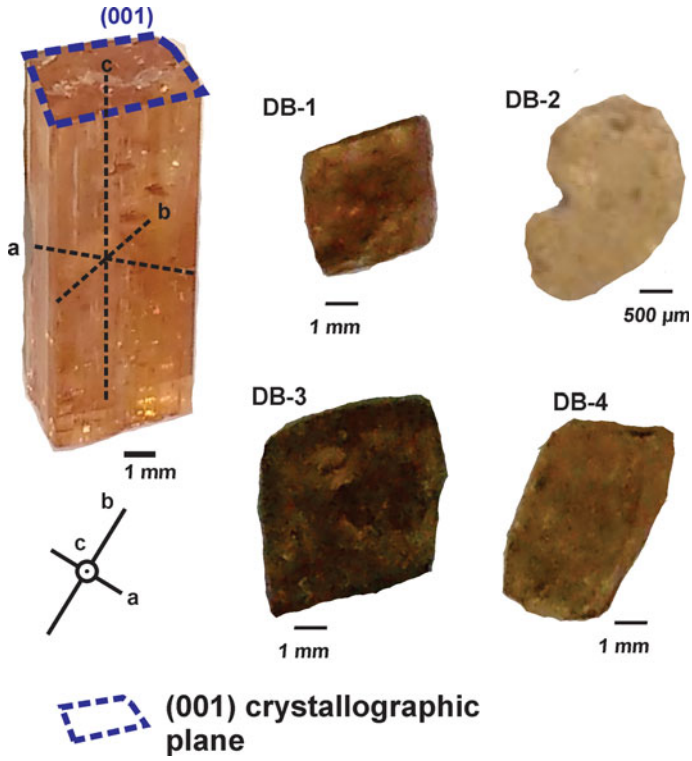

FIG. 2. Samples DB-1, DB-2, DB-3 and DB-4, cut parallel to (001). The image on the left hand side shows the orientation of crystallographic axes of euhedral topaz crystals.

Technology (CETEM), Rio de Janeiro (Brazil). It was operated at an accelerating voltage of 16 kV and beam current of 344 µA, under high vacuum conditions. A magnet was used to control the diameter of the electron beam spot at 3 µm size on the sample surface. This same equipment provided the CL spectral measurements for this study. This system contains an optical microscope model Zeiss Imager M2 m combined with a refractable parabolic mirror coated with aluminium (collecting efficiency of 75%). CL spectra in the wavelength range of 300–800 nm were recorded by a photon counting method using a photomultiplier tube and converted to digital data. Corrected CL spectra in energy units were deconvoluted into the Gaussian components corresponding to each emission centre. The standard deviation of the detector is 2.5%, fitting error of deconvolution is 5.00–10.00%.

Electron microprobe analyses

The major-element composition of imperial topaz crystals was determined by wavelength-dispersive spectroscopy (WDS), using a JEOL JXA-8230 SuperProbe 8500 at the Microanalysis Laboratory, Department of Geology in the Federal University of Ouro Preto (Brazil). The EMPA work was targeted to distinct luminescent areas identified by SEM-CL images. It used a beam current of 20 nA, an accelerating voltage of 15 kV and a spot size of 10 µm. A set of minerals were used as standards for their respective elements: augite (Si and Ca), gahnite (Al and Fe), fluorite (F), F-apatite (P) and Cr-augite (Cr). Elements were analysed for 10 to 30 s on-peak and off-peak. Relative analytical errors (1σ) of major elements are: below 1.00% for Si and for Al; and 3.00–6.00% for F.

Laser ablation inductively coupled plasma mass spectrometry (LA-ICP-MS)

Trace elements were analysed by (LA-ICP-MS) using a Thermo-Finnigan Element II, single collector sector field (SF) ICL1-MS, coupled to a CETAC UV Nd:YAG 213 nm laser with a Helix ablation cell at the Isotopic Geochemistry

https://doi.org/10.1180/minmag.2017.081.078 Published online by Cambridge University Press

Laboratory (LOPAG), Department of Geology in the Federal University of Ouro Preto, Brazil. The spot size was 40 μm. Helium combined with argon was a carrier gas and ablation was carried out with a pulse rate of 10 Hz and an energy density of 3.60 J/cm^2. The LA-ICP-MS analyses were targeted to distinct luminescence areas identified by SEM-CL images (Fig. 3), and 20 s of background acquisition was followed by 60 s of ablation. The software *GLITTER 4.0* (Macquarie University) was used for data reduction with NIST SRM610 as the primary external standard and Si as the internal standard (using the average SiO_2 content for each sample). The secondary external standard was NIST SRM612. Limits of detection (in ppm) were ~ 4.80–5.90 (Ti), 0.04–0.08 (V), 1.60–3.60 (Cr), 0.20–0.40 (Mn), 131.00–330.00 (Fe), 0.06–0.12 (Cu), 0.27–0.50 (Zn), 0.04–0.10 (Ga) and 0.43–0.73 (Ge), and the external reproducibility of results is 2 to 7%.

Raman spectroscopy

Non-destructive Raman analysis was carried out with a confocal laser Raman microscope Senterra Bruker and a cooled charge-coupled device (CCD) Peltier at the Laboratory of the Group of Environmental Technology (GRUTAM), Department of Chemistry in the Federal University of Minas Gerais (Brazil). The spectral range was 40–3700 cm^{-1}. Raman spectra were collected using 50x Olympus BX51 objectives and a frequency doubled Nd:YAG (532) He-Ne ion 20 mW monochromatic, non-polarized laser source. Beam centring and Raman calibration were performed using a Si standard (111). The laser power was set at ~30 mW. The typical spectral resolution was 2.00 cm^{-1}. All spectra were recorded at room temperature and with a light along the *c* axis of the imperial topaz samples, thus perpendicular to (001). Raman spectra were compared to the spectra from the RRUFF Database (Downs, 2006) and the literature.

Results

Cathodoluminescence

The crystals studied show different intensities of panchromatic CL, with marked brightness variations, and distinct zonation (Fig. 3). The CL-intensities, based on images obtained by SEM-CL, were divided into two categories: low and high.

The CL-panchromatic images of all samples reveal, in the crystal cores, prominent CL-zoning growth boundaries (cf. Isogami and Sunagawa, 1975; Akizuki *et al.*, 1979), specifically a central rhombic pattern. In samples DB-1 and DB-3 this central rhombic pattern can be easily observed and develops along [110]. In samples DB-2 and DB-4, the central rhombic pattern shows some elongation along [010]. In the apices of all central rhombic patterns, especially along [010], there is a common tendency to form a triangular area of very strong luminescence. In the crystal rims, it is possible to observe very dark luminescence areas, in all the samples (Fig. 3).

The OM-CL images of imperial topaz crystals displayed a low intensity blue to violet colour, which is well exemplified by the OM-CL image obtained for the sample DB-4. Due to its more evident marked luminescence area, noticed in SEM-CL images, sample DB-4 showed that the intensity variations of OM-CL and SEM-CL images do not match. The CL spectra showed a broad emission band peak with low intensity at ~417 nm (violet-blue region of the electromagnetic spectrum), and a broad emission band with high intensity and major peaks at 685, 698, 711 and 733 nm (red region of the electromagnetic spectrum; Fig. 4).

EMPA results

All samples show compositional homogeneity, with the following compositional ranges: F = 11.66–13.59 wt.%, SiO_2 = 31.41–32.37 wt.% and Al_2O_3 = 55.00–56.43 wt.% (Table 1). The ranges of Cr_2O_3, P_2O_5 and CaO are 0.01–0.15 wt.%, 0.01–0.05 wt.% and 0.01–0.05 wt.%, respectively. The high luminescence areas in panchromatic CL-images are slightly richer in F (average of 12.88 wt.%) compared to the low luminescence ones (average of 12.51 wt.%). The OH/(OH + F) ratio ranges from 0.35–0.43 ($0.72 \leq OH \leq 0.86$ apfu). Recalculation on the basis of two Al atoms indicate a slight enrichment in F (1.18–1.32 apfu) and a lower OH/(OH + F) ratio (0.35–0.41) in high luminescence areas.

LA-ICP-MS results

Some variations in the trace elements within crystals can be observed (Table 2). In all samples, Ti, V, Cr, Mn, Fe, Cu, Zn, Ga and Ge have been detected. Titanium and Cr are abundant with

https://doi.org/10.1180/minmag.2017.081.078 Published online by Cambridge University Press

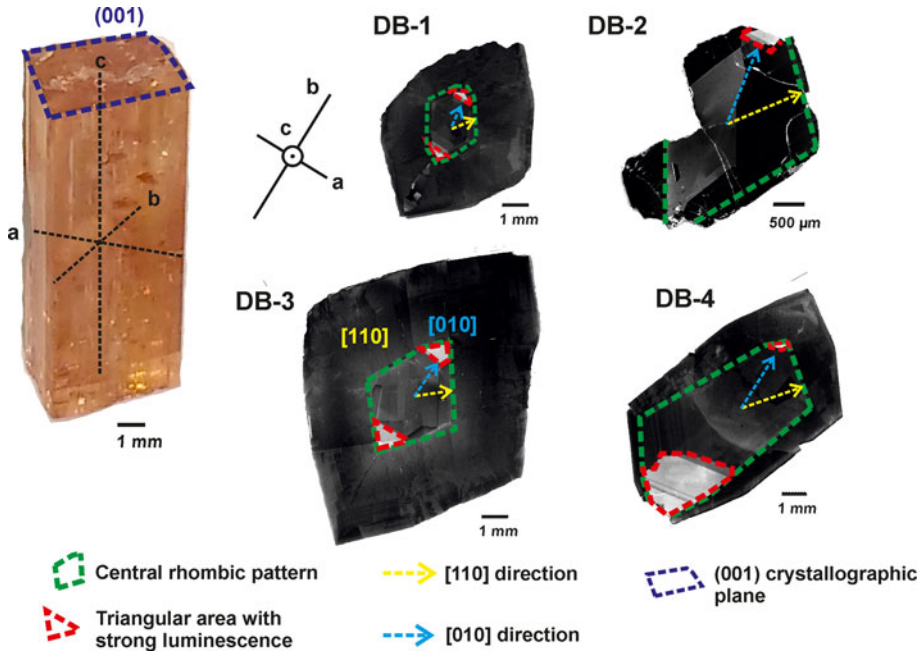

FIG. 3. SEM-CL panchromatic images of imperial topaz crystals with the following features: central rhombic pattern (green); [110] direction (yellow); triangular high luminescence area (red); and [010] direction (blue).

compositional ranges of 21.10–643.82 ppm and 21.52–887.82 ppm, respectively. Iron contents can reach thousands of ppm (352.62–1730.69 ppm), whereas other elements such as V (4.86–136.76 ppm), Mn (1.25–15.07 ppm), Cu (0.50–79.46 ppm) and Zn (2.49–79.98 ppm) are mostly of the order of a few to tens of ppm. Gallium ranges from sub-ppm to tens of ppm (0.69–20.66 ppm), but is mostly of the order of a few ppm (average 3.03 ppm). Germanium concentrations can range from a few ppm to tens of ppm (7.65–65.89 ppm), but are mostly at tens of ppm (average 29.45 ppm). Apart from the overall distribution of all these elements in the imperial topaz grains, compositions differ between the core and the rim. Titanium for instance, is slightly richer in the core (average 215.74 ppm) than the rim (average 161.92 ppm). Other elements show a similar pattern in their average concentrations: V (core 28.71 ppm / rim 23.70 ppm); Cr (core 319.42 ppm / rim 300.87 ppm); Mn (core 5.09 ppm / rim 3.65 ppm); Fe (core 799.07 ppm / rim 691.73 ppm); Cu (core 13.73 ppm / rim 10.35 ppm); Zn (core 19.75 ppm / rim 11.33 ppm); and Ge (core 35.44 ppm / rim 24.37 ppm). Gallium is richer in the rim (4.04 ppm) than in the core (1.93 ppm). Moreover, when the distribution of these elements in the core and rims are compared with luminescence characteristics, there is a correspondence with some of the elements analysed. Taking the most common ones such as Cu and Zn, which are considered as activator elements, both are considerably richer in the high luminescence core than in the rim: Cu (core 26.07 ppm / rim 6.05 ppm), Zn (core 33.91 ppm / rim 7.98 ppm) (Fig. 5).

Raman spectroscopy

In all the samples, Raman spectra were obtained in the range between 40–1600 nm. Raman spectra showed major peaks at 243, 272, 291 and 916 cm^{-1}. Secondary peaks of lower intensities were also detected at 336, 364, 405, 463, 519, 554, 642, 841 and 1160 cm^{-1} (Fig. 6). These peaks have the following assignments: symmetric Si–O ring deformation (243 cm^{-1}; Skvortsova *et al.*, 2013); various vibrational modes of $[SiO_4]$-tetrahedra (at 272, 291, 554, 841 and 916 cm^{-1}; Beny and Piriou, 1987; Downs, 2006; Skvortsova *et al.*, 2013); stretching and bending modes of $[AlO_6]$-octahedra coupled with the bending modes of $[SiO_4]$-

https://doi.org/10.1180/minmag.2017.081.078 Published online by Cambridge University Press

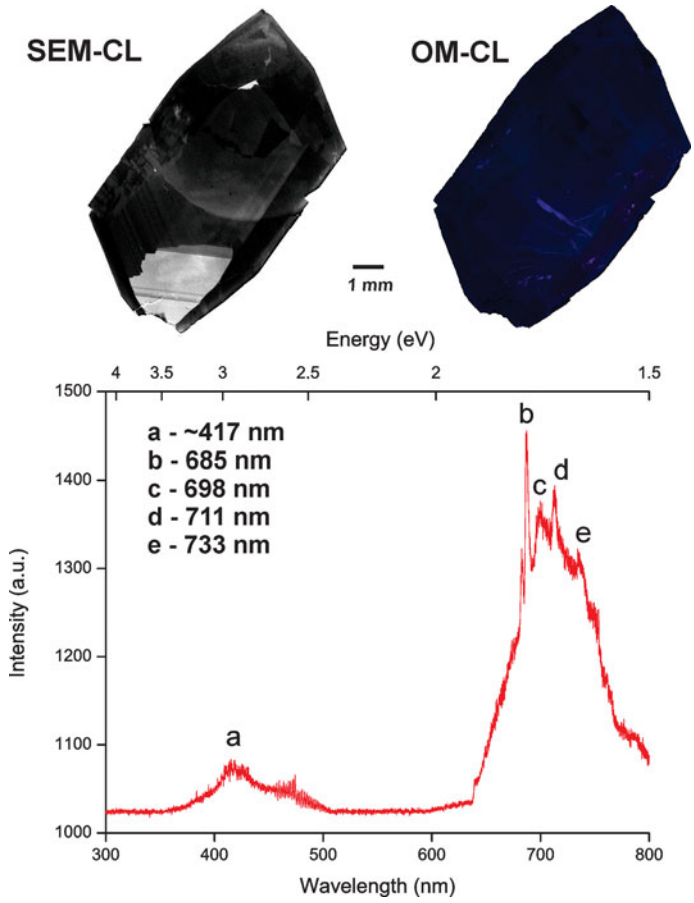

FIG. 4. Comparison of SEM-CL and OM-CL images of sample DB-4 and a CL spectrum of the same sample.

tetrahedra (at 364, 405 and 463 cm^{-1}; Beny and Piriou, 1987; Skvortsova *et al.*, 2013); stretching modes of Al–F (at 336 cm^{-1}; Agangi *et al.* 2016); in-plane bending OH-groups (at 1160 cm^{-1}; Prasad and Gowd, 2003). Even after being observed in other studies, such as Skvortsova *et al.* (2013) and Agangi *et al.* (2016), the interpretation of peaks at 519 and 642 cm^{-1} remains unclear. In our study, there was not a clear relation between the CL-bright zones and the Raman spectra.

Discussion

Compositional properties

According to Morteani *et al.* (2002), imperial topaz from Ouro Preto is assumed to be of hydrothermal origin and formed during the tectonothermal events related the Braziliano orogeny (600 Ma). The imperial topaz has a OH/(OH + F) ratio of 0.35–0.43 ($0.72 \leq OH \leq 0.86$ apfu), making it similar to topaz crystals from hydrothermal deposits (OH/(OH + F) > 0.3; Barton, 1982), and metamorphic contexts such as Sulu terrane in Eastern China ($0.35 \leq OH/(OH + F) \leq 0.55$; Zhang *et al.*, 2002). By contrast, topaz crystals of magmatic origin have a very low OH/(OH + F) ratio. For example, those from S- and A-type granites from the Krušné Hory/Erzgebirge area in Czech Republic/Germany, have a OH/(OH + F) of ~ 0.05 (Breiter *et al.*, 2013). Topaz from F-rich ongonites of the Ary-Bulak massif, Russia, have a OH/(OH + F) of ≤ 0.09 (Agangi *et al.*, 2014, 2016).

The concentrations of trace elements (Ti, V, Cr, Mn, Fe, Cu, Zn, Ga and Ge) in the imperial topaz crystals studied are here compared with topaz

https://doi.org/10.1180/minmag.2017.081.078 Published online by Cambridge University Press

TABLE 1. Representative compositions (EMPA) of imperial topaz crystals (wt.%).

Analysis	DB-1 1 rim (L)	DB-1 2 core (L)	DB-1 3 core (H)	DB-1 4 core (L)	DB-1 5 core (L)	DB-1 6 core (H)	DB-1 7 core (L)	DB-1 8 rim (L)	DB-2 1 core (H)	DB-2 2 core (H)	DB-2 3 core (L)	DB-2 4 core (L)	DB-2 5 core (L)
SiO_2	32.15	32.13	32.02	32.35	32.08	32.27	32.31	32.03	31.84	31.81	32.02	31.81	31.83
Al_2O_3	55.42	55.63	55.15	56.18	55.78	56.00	55.82	56.05	55.46	55.49	55.81	55.69	55.61
P_2O_5	0.02	n.d.	0.04	n.d.	n.d.	0.02	n.d.	n.d.	0.02	0.01	0.01	0.01	n.d.
CaO	0.01	0.02	0.01	n.d.	0.03	n.d.	n.d.	0.01	n.d.	0.01	0.02	n.d.	0.02
Cr_2O_3	0.03	0.06	0.03	0.07	0.05	0.05	0.08	0.15	0.01	n.d.	n.d.	n.d.	0.01
F	11.90	12.43	12.02	11.71	11.86	12.25	12.29	12.60	12.53	12.74	12.03	12.00	11.88
F = O	5.01	5.22	5.06	4.93	5.00	5.16	5.17	5.31	5.28	5.36	5.07	5.05	5.00
Total	99.51	100.27	99.26	100.32	99.79	100.59	100.50	100.85	99.86	100.06	99.90	99.54	99.37
Formula, apfu (2 Al)													
Si	0.99	0.99	0.99	0.99	0.99	0.99	0.99	0.99	0.99	0.99	0.99	0.99	0.99
Al	2.00	2.00	2.00	2.00	2.00	2.00	2.00	2.00	2.00	2.00	2.00	2.00	2.00
F	1.16	1.21	1.18	1.14	1.16	1.19	1.19	1.23	1.24	1.25	1.18	1.19	1.17
OH	0.85	0.82	0.83	0.86	0.85	0.83	0.82	0.78	0.77	0.78	0.83	0.83	0.83
OH/(OH + F)	0.42	0.40	0.41	0.43	0.42	0.41	0.41	0.39	0.38	0.38	0.41	0.41	0.42

Analysis	DB-2 6 core	DB-2 7 rim	DB-2 8 rim	DB-2 9 core	DB-3 1 rim	DB-3 2 rim	DB-3 3 core	DB-3 4 core	DB-3 5 core	DB-3 6 core	DB-3 7 core	DB-3 8 core	DB-3 9 rim
	(L)	(L)	(L)	(L)	(L)	(L)	(L)	(L)	(H)	(L)	(L)	(H)	(L)
SiO_2	31.88	31.85	31.60	31.65	32.11	32.24	32.31	32.28	32.30	31.98	31.42	32.37	32.04
Al_2O_3	55.47	55.89	55.49	56.14	55.63	56.17	56.09	56.43	56.41	55.88	55.00	56.06	55.95
P_2O_5	0.01	0.02	n.d.	0.03	n.d.	0.01	0.05	n.d.	n.d.	n.d.	0.02	0.02	0.03
CaO	0.01	0.03	n.d.	0.01	0.05	0.03	n.d.	n.d.	n.d.	n.d.	0.01	n.d.	0.03
Cr_2O_3	0.01	n.d.	n.d.	0.02	0.02	n.d.	0.02	0.01	n.d.	0.01	0.01	0.02	n.d.
F	12.17	12.32	11.66	12.25	12.20	12.64	13.16	12.84	13.35	13.32	12.63	13.13	12.74
F = O	5.13	5.19	4.91	5.16	5.14	5.32	5.54	5.41	5.62	5.61	5.32	5.53	5.36
Total	99.56	100.12	98.77	100.08	100.02	101.09	101.63	101.57	102.06	101.21	99.09	101.60	100.79
Formula, apfu (2 Al)													
Si	0.99	0.99	0.99	0.99	0.99	0.99	0.99	0.99	0.99	0.99	0.99	0.99	0.99
Al	2.00	2.00	2.00	2.00	2.00	2.00	2.00	2.00	2.00	2.00	2.00	2.00	2.00
F	1.19	1.20	1.16	1.21	1.19	1.22	1.27	1.25	1.29	1.29	1.25	1.27	1.24
OH	0.85	0.85	0.86	0.83	0.83	0.82	0.77	0.78	0.75	0.78	0.80	0.77	0.78
OH/(OH + F)	0.42	0.41	0.43	0.41	0.41	0.40	0.38	0.38	0.37	0.38	0.39	0.38	0.39

Analysis	DB-4 1 rim (L)	DB-4 2 core (H)	DB-4 3 core (H)	DB-4 4 core (L)	DB-4 5 core (L)	DB-4 6 core (L)	DB-4 7 core (L)	DB-4 8 rim (L)	DB-4 9 rim (L)
SiO_2	32.01	32.25	32.37	31.86	32.12	32.09	31.91	31.83	31.88
Al_2O_3	56.01	55.88	56.17	55.87	55.71	55.94	55.68	55.67	55.81
P_2O_5	0.02	0.03	n.d.	n.d.	n.d.	n.d.	n.d.	0.01	0.02
CaO	n.d.	n.d.	n.d.	n.d.	n.d.	0.01	n.d.	n.d.	n.d.
Cr_2O_3	0.04	0.02	n.d.	0.03	0.02	0.02	0.03	0.04	0.05
F	13.26	13.59	13.41	13.01	12.93	12.68	12.92	13.13	13.19
F = O	5.58	5.72	5.65	5.48	5.45	5.34	5.44	5.53	5.55
Total	101.34	101.79	101.95	100.76	100.80	100.75	100.58	100.67	100.96
Formula, apfu (2 Al)									
Si	0.99	0.99	0.99	0.99	0.99	0.99	0.99	0.99	0.99
Al	2.00	2.00	2.00	2.00	2.00	2.00	2.00	2.00	2.00
F	1.29	1.32	1.30	1.28	1.27	1.24	1.27	1.29	1.30
OH	0.74	0.72	0.72	0.73	0.74	0.80	0.77	0.73	0.73
OH/(OH + F)	0.36	0.35	0.36	0.36	0.37	0.39	0.38	0.36	0.36

(H) – high luminescence; (L) – low luminescence; n.d. – not detected.

TABLE 2. LA-ICP-MS data for imperial topaz crystals in high (HL) and low luminescence (LL) areas (ppm).

Analysis (ppm)	DB-1 1 LL	DB-1 2 LL	DB-1 3 LL	DB-1 4 LL	DB-1 5 HL	DB-1 6 HL	DB-1 7 LL	DB-1 8 LL	DB-1 9 LL	DB-2 1 HL	DB-2 2 HL	DB-2 3 LL	DB-2 4 LL	DB-2 5 LL
Ti	33.72	21.98	b.d.l.	b.d.l.	53.14	b.d.l.	24.93	57.02	364.49	204.80	643.824	576.28	b.d.l.	60.48
V	41.52	14.63	13.12	21.42	31.63	136.76	66.43	50.80	6.50	4.86	5.07	15.17	23.11	13.37
Cr	853.37	879.55	b.d.l.	337.45	377.95	b.d.l.	224.41	505.13	b.d.l.	100.99	141.48	45.04	46.58	57.55
Mn	b.d.l.	b.d.l.	b.d.l.	1.72	b.d.l.	b.d.l.	b.d.l.	1.42	b.d.l.	2.52	13.44	b.d.l.	b.d.l.	2.14
Fe	b.d.l.	b.d.l.	b.d.l.	b.d.l.	627.20	b.d.l.	b.d.l.	b.d.l.	b.d.l.	397.04	1730.70	b.d.l.	b.d.l.	390.84
Cu	7.09	4.44	15.3	6.98	37.99	16.13	11.03	11.21	14.74	47.89	6.33	0.69	2.58	6.26
Zn	4.87	3.91	3.45	6.77	25.45	18.98	5.38	12.26	14.46	16.04	17.37	2.84	b.d.l.	4.95
Ga	2.22	0.69	0.76	1.40	1.75	2.98	1.49	2.24	b.d.l.	2.10	b.d.l.	4.04	4.07	1.97
Ge	21.89	65.36	48.63	38.80	65.89	19.07	17.94	16.41	0.00	24.23	44.02	25.35	44.01	16.66

Analysis (ppm)	DB-2 6 LL	DB-3 1 LL	DB-3 2 HL	DB-3 3 HL	DB-3 4 HL	DB-3 5 LL	DB-3 6 LL	DB-4 1 LL	DB-4 2 LL	DB-4 3 LL	DB-4 4 LL	DB-4 5 HL	DB-4 6 LL
Ti	29.55	b.d.l.	b.d.l.	96.51	b.d.l.	480.22	175.21	28.42	b.d.l.	69.29	b.d.l.	b.d.l.	b.d.l.
V	8.23	51.57	b.d.l.	12.84	13.67	47.70	38.01	20.43	13.44	8.44	6.08	5.97	5.66
Cr	21.52	171.70	887.82	252.25	166.42	240.33	80.36	654.78	627.75	153.91	126.32	173.98	298.30
Mn	b.d.l.	1.44	b.d.l.	2.31	b.d.l.	15.07	2.82	2.77	2.63	b.d.l.	1.25	b.d.l.	b.d.l.
Fe	b.d.l.	b.d.l.	b.d.l.	970.93	b.d.l.	b.d.l.	b.d.l.	587.43	b.d.l.	b.d.l.	b.d.l.	b.d.l.	352.62
Cu	5.97	0.79	6.71	2.98	79.46	3.76	1.53	8.96	9.15	0.5	1.02	11.09	2.95
Zn	3.00	b.d.l.	79.98	19.58	59.97	4.86	6.04	38.51	10.48	2.49	8.73	b.d.l.	2.60
Ga	1.08	11.53	b.d.l.	2.89	0.88	b.d.l.	20.61	1.16	1.62	0.86	0.86	0.84	1.68
Ge	7.69	7.65	b.d.l.	12.57	21.07	b.d.l.	14.51	49.08	51.77	19.70	29.37	21.90	23.13

b.d.l. – below detection limit; HL – high luminescence; LL – low luminescence

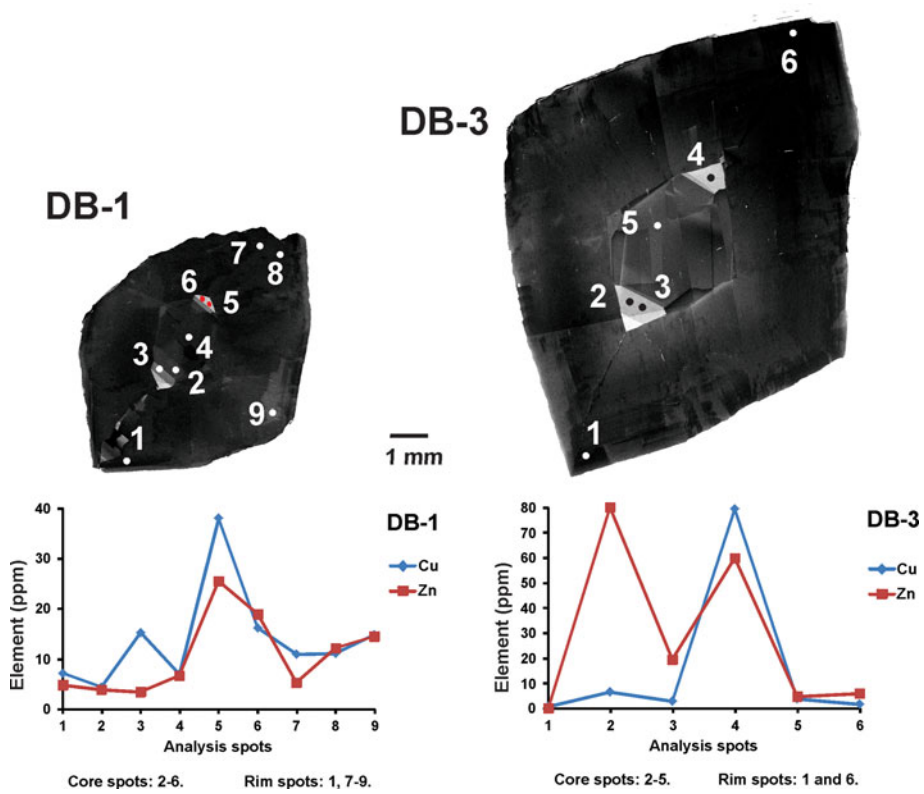

FIG. 5. SEM-CL images and their relation with Cu and Zn concentrations. Those domains with higher CL intensity are associated with higher Cu and Zn concentrations.

crystals described previously in order to establish the possible fingerprint (Table 3). The comparators are: topaz-bearing rhyolites from San Luis de Potosí, Mexico (Leroy *et al.*, 2002); a topaz- and amazonite-bearing leucogranite pluton from Xinjiang, China (Wu *et al.*, 2011); S- and A-type granites and greisens from Krušné Hory/Erzgebirge area, Czech Republic/Germany (Breiter *et al.*, 2013); and F-rich ongonites from Ary-Bulak massif, Russia (Agangi *et al.*, 2014, 2016).

The concentrations of Ti, V, Cr, Fe, Cu and Zn in imperial topaz are higher than for topaz crystals from different geological environments (Leroy *et al.*, 2002; Wu *et al.*, 2011; Wasim *et al.*, 2011; Breiter *et al.*, 2013; Agangi *et al.*, 2014, 2016). In contrast the contents of Mn, Ga and Ge in imperial topaz are lower than for other topaz crystals described previously. The Ge concentrations in the topaz crystals of S-type granite (Breiter *et al.*, 2013) and in the imperial topaz crystals of this study are mostly at tens of ppm. Notwithstanding, the average concentration of this element is more than two times greater in the S-type granites topaz (average concentration 70.52 ppm) than in the imperial topaz (average concentration 30.67 ppm).

Trace-element substitutions in the crystal structure of imperial topaz

The replacement of tetrahedral Si^{4+} by tetrahedral Ge^{4+} was demonstrated by Breiter *et al.* (2013) and Ge concentrations obtained in the present study were below 65.89 ppm. Ge^{4+} has the same charge and a similar ionic radius (Ge^{4+} 0.39 Å; Si^{4+} 0.26 Å; Shannon, 1976) as the replaced Si^{4+}. Additionally, the crystallochemical similarity between the tetrahedral Ge^{4+} and Si^{4+} in a similar topaz structure was described in a study of krieselite [$Al_2GeO_4(F,OH)_2$], a Ge-analogue of topaz (Schlüter *et al.*, 2010). Moreover, tetrahedral Ge^{4+} tends to prefer least-linked tetrahedral structures

https://doi.org/10.1180/minmag.2017.081.078 Published online by Cambridge University Press

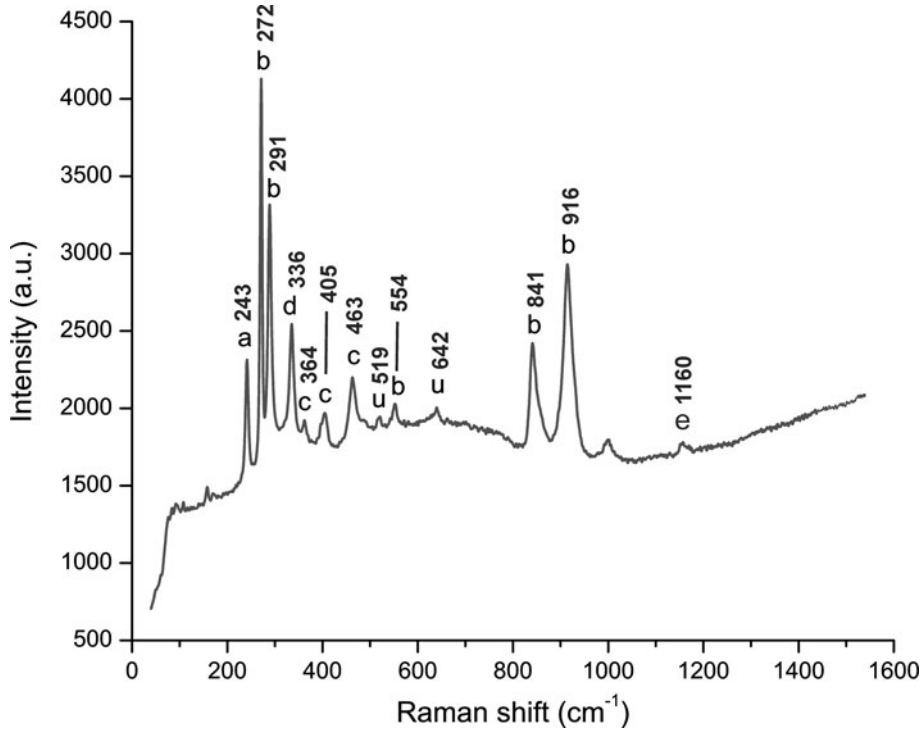

FIG. 6. Representative Raman spectrum of all imperial topaz crystals, ranging between 40–1600 nm. This spectrum was acquired in a section perpendicular to the *c* axis. The peak assignments: 'a' symmetric Si–O ring deformation; 'b' vibrational modes of [SiO_4] tetrahedra; 'c' stretching modes of [AlO_6] octahedra; 'd' stretching modes of Al–F; 'e' in-plane bending OH-groups; 'u' non assigned peaks (Beny and Piriou, 1987; Downs, 2006; Skvortsova *et al.*, 2013; Agangi *et al.*, 2016).

(Harris, 1954) and preferentially substitute tetrahedral Si^{4+} in nesosilicates (Johan *et al.*, 1983).

Octahedral Ti^{3+}, Cr^{3+}, Mn^{3+}, Fe^{3+} (Schott *et al.*, 2003) and Ga^{3+} (Breiter *et al.*, 2013; Agangi *et al.*, 2014, 2016) have substituted for octahedral Al^{3+}. The Al^{3+} has the same ionic charge and similar ionic radius (Al^{3+} 0.54 Å) to the other octahedral trivalent ions: Ti^{3+} (0.67 Å), Cr^{3+} (0.62 Å), Mn^{3+} (0.58 Å), Fe^{3+} (0.55 Å) and Ga^{3+} (0.62 Å). The valence states of Ti^{3+}, Cr^{3+}, Mn^{3+} and Fe^{3+} in imperial topaz were confirmed by EPR (Schott *et al.* (2003). In agreement with the studies carried out by Thyer *et al.* (1967), Holuj and Quick (1968) and Schott *et al.* (2003), all based on EPR results, Fe^{3+} substitutes for Al^{3+} in the crystal structure of topaz. The replacement of Al^{3+} by Ga^{3+} was described by Northrup and Reeder (1994) and Breiter *et al.* (2013). Moreover, it is important to highlight the influence of Cr as an important trace element in imperial topaz. The EPR studies of Schott *et al.* (2003) and Tarashchan *et al.* (2006) found that Cr^{3+} tends to substitute for Al^{3+}. In natural topaz crystals their luminescence is due to Cr^{3+} and to Cr^{3+}-Cr^{3+} pairs, as well as to radiation-induced centres associated with Cr (Gaft *et al.*, 2003). In agreement with Tarashchan *et al.* (2006), octahedral Cr^{3+} is responsible for intense colours and bright luminescence in imperial topaz. Specifically, those imperial topaz crystals with high Cr_2O_3 and Cr contents, obtained by EMPA and LA-ICP-MS, respectively, have stronger intensities of CL emission and the high Cr^{3+}-band emissions on Raman spectra (Fig. 7). After the excitation caused by the green Raman laser beam (532 nm), a broad red luminescence band (between 3500–3700 cm^{-1}) can be observed (Pinheiro *et al.*, 2002). In agreement with these authors, this band is related to crystal-field transitions of Cr^{3+} substituting for Al^{3+}. Also, the high concentrations of Cr in the imperial topaz crystals caused strong

https://doi.org/10.1180/minmag.2017.081.078 Published online by Cambridge University Press

https://doi.org/10.1180/minmag.2017.081.078 Published online by Cambridge University Press

TABLE 3. Comparison between the trace-element composition of imperial topaz and topaz crystals from different geological environments (ppm).

	Environment	Ti	V	Cr	Mn	Fe	Cu	Zn	Ga	Ge
Leroy *et al.* (2002)	Rhyolite	n.a.	10^{-1}–10^{0}	10^{0}–10^{1}	n.a.	n.a.	mostly 10^{0}	mostly 10^{0}	10^{0}–10^{1}	n.a.
Wasim *et al.* (2011)	Pegmatite	n.a.	n.a.	mostly 10^{0}	mostly 10^{0}	mostly 10^{2}	n.a.	n.a.	10^{0}–10^{1}	10^{1}–10^{2}
	Hydrothermal vein	n.a.	n.a.	n.a.	n.a.	n.a.	n.a.	mostly 10^{0}	mostly 10^{0}	mostly 10^{2}
Wu *et al.* (2011)	Granite	n.a.	n.a.	n.a.	n.a.	n.a.	n.a.	n.a.	n.a.	n.a.
Breiter *et al.* (2013)	S-type granite	n.a.	n.a.	n.a.	n.a.	10^{1}–10^{2}	n.a.	n.a.	10^{0}–10^{1}	mostly 10^{1} 70.52 ppm *
	A-type granite	n.a.	n.a.	n.a.	n.a.	10^{0}–10^{2}	n.a.	n.a.	mostly 10^{0}	10^{1}–10^{2}
	Greisen	n.a.	n.a.	n.a.		n.a.	n.a.	n.a.	10^{0}–10^{1}	10^{1}–10^{2}
Agangi *et al.* (2014, 2016)	Ongonite	10^{0}–10^{1}	10^{-1}–10^{0}	bdl	mostly 10^{1}	10^{1}–10^{2}	mostly bdl	10^{-1}–10^{0}	10^{0}–10^{1}	n.a.
Our study	Hydrothermal vein	10^{1}–10^{2}	10^{0}–10^{1}	10^{1}–10^{2}	mostly 10^{0}	10^{2}–10^{3}	10^{0}–10^{1}	10^{0}–10^{1}	10^{-1}–10^{0}	mostly 10^{1} 30.67 ppm *

*Average calculated content; n.a. – not analysed; bdl – below detection limit.

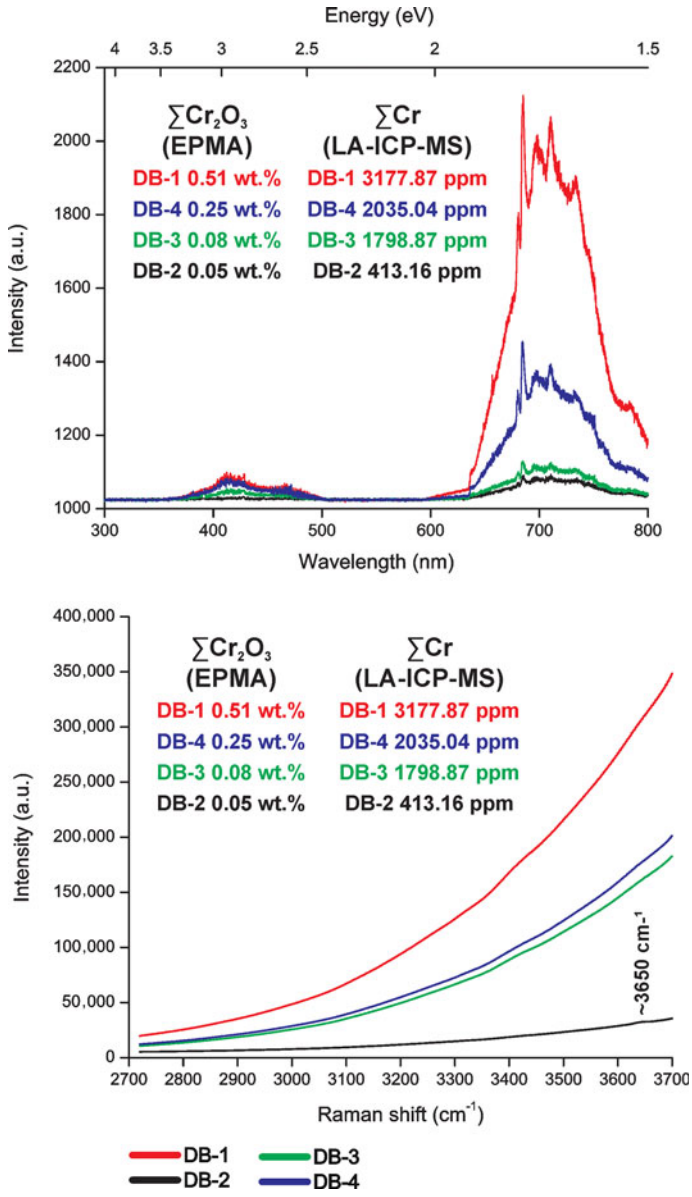

FIG. 7. A comparison between CL and Raman spectroscopy results of imperial topaz crystals, according to their $\sum Cr_2O_3$ and $\sum Cr$ concentrations obtained by EMPA and LA-ICP-MS, respectively.

luminescence intensities superimposed on the ~3650 cm^{-1} peak related to the OH-stretching modes (Beny and Piriou, 1987; Fig. 6). Only in the Raman spectrum of the sample DB-2, with the lower Cr concentrations, can an incipient peak be seen at ~3650 cm^{-1} (Fig. 7).

Substitution of major elements by elements of different ionic charge also occurs in imperial topaz. Octahedral V^{4+} (Schott *et al.*, 2003), Ti^{4+} (Northrup and Reeder, 1994; Schott *et al.*, 2003), Cu^{2+} and Zn^{2+} can substitute for octahedral Al^{3+}. Schott *et al.* (2003) revealed that OH groups show a higher tendency for polarization than F ions and, hence, two F ligands increase the ionic character of the V^{4+} ligand. The octahedral coordinated V^{4+} is more likely to be detected by EPR at room temperature

https://doi.org/10.1180/minmag.2017.081.078 Published online by Cambridge University Press

than tetrahedral coordinated V^{4+}, which occurs at temperatures below –213.15°C (Schott *et al.*, 2003). Due to its large dimension, octahedral Ti^{4+} is more likely to substitute for Al^{3+} than tetrahedral Si^{4+}; in addition in topaz, this substitution can also happen with charge compensation by O^{2-} for F^{-} (Northrup and Reeder 1994). Ti^{4+} and V^{4+} can also enter into the crystal structure of topaz because of their high ionic potential (6.61 and 6.90, respectively; Shannon, 1976), when compared to ionic potential of Al^{3+} (5.61). The replacement of octahedral Al^{3+} for octahedral Mn^{2+}, Cu^{2+} and Zn^{2+} can occur, because these ions present low ionic potentials (2.41, 2.74 and 2.70, respectively). This substitution occurs due to the low charge of Cu^{2+} and Zn^{2+} or to the large ionic radii (0.73 Å and 0.74 Å, respectively), or even both. Zn^{2+} can be introduced into the imperial topaz crystal structure because of its tendency to form a relatively higher proportion of ionic bonds with OH^{-} ligands (Albarède, 2004), which are part of the crystal structure of topaz. According to Misra (2012), octahedral Cu^{2+} is taken up by the minerals that crystallize during the late stage of a rock crystallization process. Topaz is related to late stages of crystallization, which can allow the incorporation of small quantities of Cu^{2+} in its crystal structure.

Cathodoluminescence properties

The luminescence of an ion will depend on the interactions with other constituents of the crystal structure, the crystallographic site of the elements considered and on the crystal field. When the crystal field is strong, the luminescence emission will show broad emission bands (Götze, 2000, 2012). According to Stevens-Kalceff (2009), the incorporation of transition metals (Ti, V, Cr) in topaz results in broader luminescence peaks, which is consistent with the obtained peaks at 685, 698, 711 and 733 nm (Fig. 3). In agreement with Gaft *et al.* (2003, 2005), these peaks are related to a transition metal, especially Cr^{3+}. The broad emission band with low intensity peak at ~417 nm can be interpreted as point defects, due to intrinsic luminescence centres. In our case, this broad featureless part of the CL spectra can be related to point defect centres such as vacancies or interstitial clusters.

Images of quartz and topaz using SEM-CL have been crucial for understanding the crystallization dynamics of these minerals and their geological setting (e.g. hydrothermal, metamorphic environment; Boggs *et al.* 2002; Van den Kerkhof *et al.* 2004; Rusk *et al.* 2008; Götte *et al.*, 2011; Agangi *et al.* 2014; Frelinger *et al.* 2015; Agangi *et al.* 2016). The central rhombic pattern, observed in the CL-panchromatic images of the cores of all samples, shows that this area was marked by multiple precipitation-dissolution events, which are representative of physicochemical changes within the hydrothermal system. In the rims are very dark luminescence areas, which are truncated by some irregular-shaped areas. These textures can be related to metamorphic activity, shown by lower CL along the rims of the grain, which can imply recrystallization and some removal of impurities thus producing a homogeneous CL response. Moreover, the growth speed, combined with the configuration of cation sites and the incorporation of trace elements, could produce sectoral differences (Gatta *et al.*, 2006). In addition, all these crystallization features, showed by the CL-panchromatic images, suggest a primary process of crystallization followed by a process of recrystallization.

Finally, it is also noticeable that high concentrations of Cu and Zn can suggest a CL-activator role in imperial topaz. The role of the high concentrations of Cu and Zn, namely as octahedral Cu^{2+} and Zn^{2+}, as CL-activators can be explained by Fig. 6. Also, replacement of octahedral Al^{3+} by octahedral Cu^{2+} and Zn^{2+}, due to the differences between ionic charge and radii, may have strongly influenced the local electronic framework of the crystal structure and, consequently, affected the luminescence emissions.

Conclusions

The textures and compositional zoning of imperial topaz provide important information about its evolution. The SEM-CL images show intracrystalline luminescence variations and different CL-textures that indicate a primary process of crystallization followed by a process of recrystallization. This process can also be related to the metamorphic tectonothermal event that occurred during the Brasiliano orogeny in the region of Ouro Preto, at ~600 Ma (Morteani *et al.*, 2002). Colour CL images indicate only blue to violet emissions. The CL-spectra indicate a broad emission band with low intensity peak at ~417 nm, and a broad emission band with high intensity and major peaks at 685, 698, 711 and 733 nm. It is likely that the substitution of trace elements in the structure of imperial topaz caused point defect centres as a lattice distortion; which produced the peak at

https://doi.org/10.1180/minmag.2017.081.078 Published online by Cambridge University Press

~417 nm. This hypothesis can be supported by the high concentrations of Cu and Zn in the areas of high luminescence intensity. Moreover, Raman and CL-spectra indicate high Cr concentrations, corroborated by EMPA and LA-ICP-MS results. The high Cr caused strong luminescence intensities that generated a superimposition over the ~3650 cm^{-1} peak, related to the OH-stretching mode of topaz in all Raman spectra.

Finally, our results show the chemical fingerprint of imperial topaz is high concentrations of Ti and Cr (tens to hundreds of ppm), V, Cu and Zn (few to tens of ppm), and Fe (tens to hundreds of ppm), and low concentrations of Mn (mostly few ppm), Ga (sub-ppm to few ppm) and Ge (mostly tens of ppm, average of 30.67 ppm).

Acknowledgements

Mr Edmar Silva, Mr André Silva and Mr Hélio Bezerra are thanked for providing sample material for our study. Mr. Marco Silva is thanked for the preparation of the samples. Prof. Dr Cristiano Lana (Federal University of Ouro Preto) and MSc Fernando Vasques (CETEM) are thanked for analytical assistance on the LA-ICP-MS and CL-spectroscopy, respectively. This project acknowledges support from the Isotopic Geochemistry Laboratory of the Federal University of Ouro Preto (APQ03943). Microanalysis Laboratory of the Federal University of Ouro Preto, a member of the Microscopy and Microanalysis Network of Minas Gerais State/Brazil/FAPEMIG, is thanked for the mineral chemistry analyses. The authors are specially thanked to Prof Dr Jens Götze (TU Bergakademie Freiberg, Germany), Prof Dr Ricardo Scholz (Federal University of Ouro Preto) and MSc Francesco Narduzzi (Federal University of Ouro Preto) for very helpful comments and literature suggestions to this manuscript. MSc Hugo Moreira (University of Portsmouth) is thanked for helpful discussions and for the photos taken in the Dom Bosco mine.

References

Agangi, A., Kamenetsky, V.S., Hofmann, A., Przybyłowicz, W. and Vladykin, N.V. (2014) Crystallisation of magmatic topaz and implications for Nb-Ta-W mineralisation in F-rich silicic melts – The Ary-Bulak ongonite massif. *Lithos*, **202–203**, 317–303.

Agangi, A., Gucsik, A., Nishido, H., Ninagawa, K. and Kamenetsky, V.S. (2016) Relation between cathodoluminescence and trace-element distribution of magmatic topaz from the Ary-Bulak massif, Russia. *Mineralogical Magazine*, **80**(5), 881–899.

Akizuki, M., Hampar, M.S. and Zussman, J. (1979) An explanation of anomalous optical properties of topaz. *Mineralogical Magazine*, **43**, 237–241.

Albarède, F. (2004) The stable isotope geochemistry of copper and zinc. Pp. 409–427 in: *Geochemistry of Non-Traditional Stable Isotopes* (C.M. Johnson, B.L. Beard and F. Albarede, editors). Reviews in Mineralogy & Geochemistry, **55**. Mineralogical Society of America and the Geochemical Society, Washington, DC.

Alberico, A., Ferrando, S., Ivaldi, G. and Ferraris, G. (2003) X-ray single-crystal structure refinement of an OH-rich topaz from Sulu UHP terrane (Eastern China) – Structural foundation of the correlation between cell parameters and fluorine content. *European Journal of Mineralogy*, **15**, 875–881.

Alkmim, F.F. and Marshak, S. (1998) Transamazonian orogeny in the Southern São Francisco Craton Region, Minas Gerais, Brazil: evidence for Paleoproterozoic collision and collapse in the Quadrilátero Ferrífero. *Precambrian Research*, **90**, 29–58.

Babinski, M., Chemale, F., van Schumus, W.R. (1995) The Pb/Pb age of Minas Supergroup carbonate rocks, Quadrilátero Ferrífero, Brazil. *Precambrian Research*, **72**, 235–245.

Barton, M.D. (1982) The thermodynamic properties of topaz solid solutions and some petrologic applications. *American Mineralogist*, **67**, 956–974.

Beny, J.M. and Piriou, B. (1987) Vibrational spectra of single-crystal topaz. *Physics and Chemistry of Minerals*, **15**, 148–154.

Boggs, S.J., Kwon, Y.-I., Goles, G.G., Rusk, B.G., Krinsley, D. and Seyedolali, A. (2002) Is quartz cathodoluminescence color a reliable provenance tool? A quantitative examination. *Journal of Sedimentary Research*, **72**, 408–415.

Breiter, K., Gardenová, N., Vaculovič, T. and Kanický, V. (2013) Topaz as an important host for Ge in granites and greisens. *Mineralogical Magazine*, **77**, 403–417.

Dorr II, J.V.N. (1969) *Physiographic, stratigraphic and structural development of the Quadrilátero Ferrífero, Minas Gerais, Brazil: U.S.* Geological Survey Professional Paper 641-A. United States Government Printing Office, Washington D.C., USA, 109 pp.

Downs, R.T. (2006) The RRUFF Project: an integrated study of the chemistry, crystallography, Raman and infrared spectroscopy of minerals. Pp. 3–13 in: *Program and Abstracts of the 19th General Meeting of the International Mineralogical Association, Kobe, Japan*.

Frelinger, S.N., Ledvina, M.D., Kyle, J.R. and Zhao, D. (2015) Scanning electron microscopy cathodoluminescence of quartz: principles, techniques and applications in ore geology. *Ore Geology Reviews*, **65**, 840–852.

https://doi.org/10.1180/minmag.2017.081.078 Published online by Cambridge University Press

Gaft, M., Nagli, L., Reisfeld, R., Panczer, G. and Brestel, M. (2003) Time-resolved luminescence of Cr^{3+} in topaz $Al_2SiO_4(OH,F)_2$. *Journal of Luminescence*, **102–103**, 349–356.

Gaft, M., Reisfeld, R. and Panczer, G. (2005) *Modern Luminescence Spectroscopy of Minerals and Materials*. Springer-Verlag, Heidelberg, Germany, 356 pp.

Gaines, R.V., Skinner, H.C.W., Foord, E.E., Mason, B., Rosenzweig, A. and King, V.T. (1997) *Dana's New Mineralogy (8th edition)*. John Wiley & Sons, New York, USA, 1819 pp.

Gandini, A.L. (1994) *Mineralogia, inclusões fluidas e aspetos genéticos do topázio imperial da região de Ouro Preto, Minas Gerais.* MSc dissertation, University of São Paulo, São Paulo, 212 pp.

Gatta, G.D., Nestola, F., Bromiley, G.D. and Loose, A. (2006) New insight into crystal chemistry of topaz: a multi-methodological study. *American Mineralogist*, **91**, 1839–1846.

Götte, T., Pettke, T., Ramseyer, K., Koch-Müller, M. and Mullis, J. (2011) Cathodoluminescence properties and trace element signature of hydrothermal quartz: a fingerprint of growth dynamics. *American Mineralogist*, **96**, 802–813.

Götze, J. (2000) Cathodoluminescence in applied geosciences. Pp. 457–477 in: *Cathodoluminescence in Geosciences* (M. Pagel, V. Barbin, P. Blanc and D. Ohnenstetter, editors). Springer-Verlag, Heidelberg, Germany.

Götze, J. (2012) Application of cathodoluminescence microscopy and spectroscopy in geosciences. *Microscopy and Microanalysis*, **18**, 1270–1284.

Harris, P.G. (1954) The distribution of germanium among coexisting phases of partly glassy rocks. *Geochimica et Cosmochimica Acta*, **5**, 185–195.

Holuj, F. and Quick, S.M. (1968) ESR spectrum of Fe^{3+} in topaz. II. Superhyperfine structure. *Canadian Journal of Physics*, **46**, 1087–1099.

Isogami, M. and Sunagawa, I. (1975) X-ray topographic study of a topaz crystal. *American Mineralogist*, **60**, 889–897.

Johan, Z., Oudin, E. and Picot, P. (1983). Analogues germanifères et gallifères des silicates et oxydes dans les gisements de zinc des Pyrénées centrales, France; argutite et carboirite, deux nouvelles espèces minerales. *Tschermaks Mineralogische un Petrographische Mitteilungen*, **31**, 97–119.

Lana, C., Alkmim, F.F., Armstrong, R., Scholz, R., Romano, R. and Nalini Jr., H.A. (2013) The ancestry and magmatic evolution of Archaean TTG rocks of the Quadrilátero Ferrífero province, Southeast Brazil. *Precmbrian Research*, **231**, 157–173.

Leroy, J.L., Rodríguez-Rios, R. and Dewonck, S. (2002) The topaz-bearing rhyolites from the San Luis Potosi area (Mexico): characteristics of the lava and growth conditions of topaz. *Bulletin de la Société Géologique de France*, **173**, 579–588.

Machado, N. and Carneiro, M. (1992) U-Pb evidence of Late Archean tectonothermal activity in southern São Francisco shield, Brazil. *Canadian Journal of Earth Sciences*, **29**, 2341–2346.

Machado, N., Noce, C.M., Ladeira, E.A. and Oliveira, O.A. B. (1992) U-Pb geochronology of the Archean magmatism and Proterozoic metamorphism in the Quadrilátero Ferrífero, southern São Francisco Craton, Brazil. *Geological Society of America Bulletin*, **104**, 1221–1227.

Marshall, D. and Walton, L. (2007) Topaz. Pp. 161–168 in: *Geology of Gem Deposits* (L.A. Groat, editor). Short Course Series, **37**. Mineralogical Association of Canada, Vancouver, British Columbia, Canada.

Misra, K.C. (2012) *Introduction to Geochemistry: Principles and Applications*. Wiley-Blackwell, New Jersey, 452 pp.

Morteani, G., Bello, R.M.S., Gandini, A.L. and Preinfalk, C. (2002) P, T, X conditions of crystallization of Imperial Topaz from Ouro Preto (Minas Gerais, Brazil): fluid inclusions, oxygen isotope thermometry and phase relations. *Schweizerische Mineralogische und Petrographische Mitteilungen*, **82**, 455–466.

Noce, C.M., Machado, N. and Teixeira, W. (1998) U-Pb geochronology of gneisses and granitoids in the Quadrilátero Ferrífero (Southern São Francisco Craton): age constraints for Archaean and Paleoproterozoic magmatism and metamorphism. *Revista Brasileira de Geociências*, **28**, 95–102.

Northrup, P.A. and Reeder, R.J. (1994) Evidence for the importance of growth-surface structure to trace element incorporation in topaz. *American Mineralogist*, **79**, 1167–1175.

Olsen, D.R. (1971) Origin of topaz deposits near Ouro Preto, Minas Gerais, Brazil. *Economic Geology*, **66**, 627–631.

Pinheiro, M.V.B., Fantini, C., Krambrock, K., Persiano, A. I.C., Dantas, M.S.S. and Pimenta, M.A. (2002) OH/F substitution in topaz studied by Raman spectroscopy. *Physical Review B*, **65**, 104301.

Prasad, P.S.R. and Gowd, T.N. (2003) FTIR spectroscopic study of hydroxyl ions in natural topaz. *Journal of the Geological Society of India*, **61**, 202–208.

Renger, F.E., Noce, C.M., Romano, A.W. and Machado, N. (1995) Evolução sedimentar do Supergrupo Minas: 500 Ma de registro geológico no Quadrilátero Ferrífero, Minas Gerais, Brasil. *Geonomos*, **2**, 1–11.

Rusk, B.G., Lowers, H.A. and Reed, M.H. (2008) Trace elements in hydrothermal quartz: relationships to cathodoluminescent textures and insights into vein formation. *Geology*, **36**, 547.

Schlüter, J., Geisler, T., Pohl, D. and Stephan, T. (2010) Krieselite, $AL_2GeO_4(F,OH)_2$: a new mineral from the Tsumeb mine, Namibia, representing the Ge analogue of

https://doi.org/10.1180/minmag.2017.081.078 Published online by Cambridge University Press

topaz. *Neues Jahrbuch für Mineralogie, Abhandlungen*, **187**, 33–40.

Schott, S., Rager, H., Schürmann, K. and Taran, M. (2003) Spectroscopic study of natural gem-quality "Imperial" topazes from Ouro Preto, Brazil. *European Journal of Mineralogy*, **15**, 701–706.

Shannon, R.D. (1976) Revised effective ionic radii and systematic studies of interatomic distances in halides and chalcogenides. *Acta Crystallographica*, **A32**, 751–767.

Silva, J.C. and Ferreira, C.M. (1987). *Gemas do Brasil (Gems of Brazil)*. São Bernardo do Campo (SP), Brazil, 130 pp.

Skvortsova, V., Mironova-Ulmane, N., Trinkler, L. and Chikvaidze, G. (2013) Optical properties of natural topaz. *Materials Science and Engineering*, **49**, 1–4.

Stevens-Kalceff, M.A. (2009) Cathodoluminescence microcharacterization of point defects in α-quartz. *Mineralogical Magazine*, **73**, 585–605.

Tarashchan, A.N., Taran, M.N., Rager, H. and Iwanuch, W. (2006) Luminescence spectroscopic study of Cr^{3+} in Brazilian topazes from Ouro Preto. *Physics and Chemistry of Minerals*, **32**, 679–690.

Thyer, J.R., Quick, S.M. and Holuj, F. (1967) ESR spectrum of Fe^{3+} in topaz: I. fine structure. *Canadian Journal of Physics*, **45**, 3597–3610.

Van der Kerkhof, A.M., Kronz, A., Simon, K. and Scherer, T. (2004) Fluid-controlled quartz recovery in granulite as revealed by cathodoluminescence and trace element analysis (Bamble sector, Norway). *Contributions to Mineralogy and Petrology*, **146**, 637–652.

Wasim, M., Zafar, W.A., Tufail, M., Arif, M., Daud, M. and Ahmad, A. (2011) Elemental analysis of topaz from northern areas of Pakistan and assessment of induced radioactivity level after neutron irradiation for color induction. *Journal of Radioanalytical and Nuclear Chemistry*, **287**, 821–826.

Wu, C.-Z., Liu, S.-H., Gu, L.-X., Zhang, Z.-Z. and Lei, R.-X. (2011) Formation mechanism of the lanthanide tetrad effect for a topaz- and amazonite-bearing leucogranite pluton in eastern Xinjiang, NW China. *Journal of Asian Earth Sciences*, **42**, 903–916.

Wunder, B., Rubie, D.C., Ross II, C.R., Medenbach, O., Seifert, F. and Schreyer, W. (1993) Synthesis, stability, and properties of $Al_2SiO_4(OH)_2$: a full hydrated analogue of topaz. *American Mineralogist*, **78**, 285–297.

Wunder, B., Andrut, M. and Wirth, R. (1999) High-pressure synthesis and properties of OH-rich topaz. *European Journal of Mineralogy*, **11**, 803–813.

Zhang, R.Y., Liou, J.G. and Shu, J.F. (2002) Hydroxyl-rich topaz in high-pressure and ultrahigh-pressure kyanite quartzites, with retrograde woodhouseite, from the Sulu terrane, eastern China. *American Mineralogist*, **87**, 445–453.

https://doi.org/10.1180/minmag.2017.081.078 Published online by Cambridge University Press